Carbon 142 (2019) 388–400

Contents lists available at ScienceDirect

Carbon

journal homepage: www.elsevier.com/locate/carbon

Strength of graphene grain boundaries under arbitrary in-plane tension

Andy Fox, Upamanyu Ray, Teng Li*

Department of Mechanical Engineering, University of Maryland, College Park, MD, 20742, United States

ARTICLE INFO

Article history:
Received 7 July 2018
Received in revised form
17 October 2018
Accepted 19 October 2018
Available online 23 October 2018

ABSTRACT

Understanding the tensile strength of graphene grain boundaries (GBs) is crucial for correlating the mechanical properties of two dimensional polycrystalline graphene with its atomic defect structure, a key to the success of large area graphene in many promising applications. Existing modeling studies mainly focus on the deformation and fracture of graphene GBs under tension that is perpendicular to the GBs. In reality, however, when a polycrystalline graphene is subject to a simple tension, random distribution of GBs in the graphene leads to arbitrary in-plane loading conditions of the GBs that cannot be fully understood with existing knowledge. To this end, we carry out systematic molecular dynamics (MD) simulations and also delineate a continuum mechanics model to investigate the failure strength of graphene GBs under tension in all possible loading directions. Particular focus is placed on quantitatively deciphering the interplay between GB misorientation angle and loading angle, and their effects on the failure strength of graphene GBs. Prediction from the continuum mechanics model based on a disclination dipole theory agrees well with the results from MD simulations. In this sense, the present study offers important insights on a better understanding of the mechanical properties of large area polycrystalline graphene.

1. Introduction

The widespread use of graphene-based devices and materials [1–4] relies on mass production of large area graphene. Chemical vapor deposition (CVD) has been shown to be a facile approach to growing large area monolayer graphene [5–8]. In such a growth process, individual graphene crystals first nucleate on individual grains of a metallic substrate, with random crystalline orientation, then grow until meeting and coalescing with neighboring crystals. Therefore the resulting CVD-grown graphene is polycrystalline [9], with misaligned boundaries between neighboring graphene grains. Such graphene grain boundaries (GBs) are essentially line defects (e.g., often in the form of strings of pentagon-heptagon edge dislocations [10–13], and play important roles on the mechanical [14–17], thermal [18,19], electrical properties [20–22] of the resulting polycrystalline graphene. For example, it has been shown that, the strength of graphene with large-angle GBs (more misoriented) are even higher than that of graphene with low-angle GBs, an anomalous feature distinct from GBs in typical materials [23]. Further studies have shown that, in addition to the defect densities [24–26], the nature of arrangement of the GB defects also plays a key role in either strengthening or weakening graphene [17,27–34]. A better understanding of the graphene GB enables defect engineering to modulate mechanical properties such as strength [35–40], fracture toughness [41–45], wrinkling [46], crack formation [47–49] and mechanical mutability [50].

The exceptional intrinsic mechanical and electronic properties of graphene motivate the development of graphene-based high performance electronic devices with superb mechanical deformability and durability, such as flexible and stretchable electronics [51–53]. Enthusiasm aside, the existing knowledge of the mechanics of GBs in graphene falls short in offering a comprehensive understanding of the mechanical properties of polycrystalline graphene. For example, when an electrode made of polycrystalline graphene in a stretchable electronic device is subject to uniaxial tension, the GBs in the polycrystalline graphene is indeed subject to in-plane tension in various directions, given the random orientation of GBs. However, most existing investigations on the strength of graphene GB only consider a tensile loading applied either perpendicular or parallel to the GB [23,54–58]. Findings from such

* Corresponding author.
E-mail address: lit@umd.edu (T. Li).

https://doi.org/10.1016/j.carbon.2018.10.065
0008-6223/

investigations shed light on the strength of graphene GBs but fall short in predicting the deformation behavior and failure mechanism of a polycrystalline graphene in practical applications. Aiming to fill such a knowledge gap on the strength of graphene GBs, here we present a comprehensive study of the strength of graphene GBs under arbitrary in-plane tension, using both a modified continuum model and molecular dynamics simulations. The rest of the paper is organized as follows. Section 2 describes the atomistic configurations of graphene tilt GB in full spectrum of the misorientation angle. Section 3 reports a comprehensive molecular dynamics (MD) study of the failure mode and failure strength of all graphene tilt GBs defined in Section 2 under arbitrary in-plane tension. Section 4 delineates a continuum mechanics model based on disclination dipole theory to predict GB strength, the results from which are compared with those from MD simulations in Section 5. Major findings of the present study are summarized in Section 6.

2. Configurations of graphene tilt GB

We consider a graphene tilt GB formed between two single crystalline graphene grains with a misorientation angle θ (Fig. 1a), subject to an in-plane tension with a loading angle ϕ as defined in Fig. 1b.

We study the strength of such a tilt GB under arbitrary in-plane tension, ranging from $\phi = 0^\circ$ (perpendicular to GB) to 90° (parallel to GB). Fig. 2 plots all possible graphene GB configurations (in total of 24) with a misorientation angle ranging from 2.1° to 54.3°. Depending on the structural features, the 24 GB configurations can be grouped into three categories. For the range of misorientation angle θ from 2.1° to 21.8°, the GB features a periodic array of disclination dipoles (1dp) made of a pentagon-heptagon defect or dipole clusters (made of 2 or 3 dipoles, e.g., 2dp, 3dp) (Fig. 2a). GBs in this category are termed as armchair oriented GBs (AC GBs). For the range of θ from 32.2° to 54.3°, the GB features a periodic array of disclination clusters made of a pentagon-heptagon-pentagon-heptagon defect (Fig. 2c). GBs in this category are termed as zigzag oriented GBs (ZZ GBs). For the intermediate range of misorientation angle from 23.3° to 30.2°, the GBs show mixed features of AC and ZZ GBs, termed as transition GBs.

3. Molecular dynamics study of the strength of AC and ZZ GBs of graphene

We use the Large-scale Atomic/Molecular Massively Parallel Simulator (LAMMPS) [60] for the MD study of the strength of graphene GBs. The size of the simulation model, on one hand, needs to be large enough to contain enough defects along the GB, and on the other hand, needs to be suitable so that parametric studies of GB properties are not computation time prohibitive. For such considerations, in all simulations, the polycrystalline graphene is in a size of 120 Å × 120 Å. While fixing the x, y, and z displacement of atoms in a small section of the sheet in the lower left corner of the sheet, and also fixing the displacement of atoms in a narrow strip of the entire left and right boundary in the x and z directions, the entire structure is energy minimized, allowing the structure to relax to its lowest energy state and ensuring stable bonding among all the atoms. From there an assigned displacement is incrementally applied to one end of the graphene sheet with a strain rate of 5×10^8/second until tensile fracture occurs while the other end is fixed. We adopt the adaptive intermolecular reactive bond order (AIREBO) potential [61] to model the interaction of the carbon atoms and their bond breaking and formation. This potential has been used extensively [10,17,23,24,27,54,58,62,63] to study GBs in graphene since it matches well with first principle calculations and experimental results. Following [23,24], we adopt a carbon–carbon covalent interaction cutoff distance of 1.92 Å to avoid spuriously high failure strengths. A Berendsen thermostat with a velocity-Verlet time stepping scheme is used in the simulations and the structure is initialized at a temperature of 300K. The time step is 0.001ps. Virial stresses for each atom are calculated. For each GB configuration, we simulate its tensile failure under 12 different loading angles, namely, 0°, 10°, 20°, 25°, 30°, 40°, 45°, 50°, 60°, 70°, 80°, and 90°. For each of the 24 GB configurations and each of the 12 loading angles, 10 simulation cases are carried out and the mean and standard deviation of the GB tensile strength are obtained. In total, 2880 simulation cases are carried out, yielding the results as follows.

Serpentine GBs have been observed in experiments [40], but the atomic structure for this study are only for one ideal straight GB between two grains. There are many methods that can be used to determine the atomic structure of GBs such as phase-field crystal (PFC) modeling [64,65], the coincidence site lattice (CSL) method [66], density functional theory (DFT) calculations [38,62,66], force-field calculations [66], and another method like CSL using Moire' patterns [28]. Studies on straight GBs produce similar atomic GB arrangements where the defect density increases as θ increases to ~30°, then the defect density decreases as it goes to 60°. For this study, points representing atoms were arranged into approximately the atomic configuration shown in Fig. 2 using Matlab. These atomic arrangements were chosen because they were the most commonly seen in previous studies [10,23,24,27,38,59,67]. Then an energy minimization of the system was performed using LAMMPS to determine the initial state of the sheets by iteratively adjusting atom coordinates, which also allowed the structure to buckle in the z direction to find its lowest energy state. The minimization style used was the Polak-Ribiere version of the conjugate gradient (CG) algorithm for 40,000 iterations. Non-periodic boundary conditions were used on all sides. One study using PFC [64] produced GBs

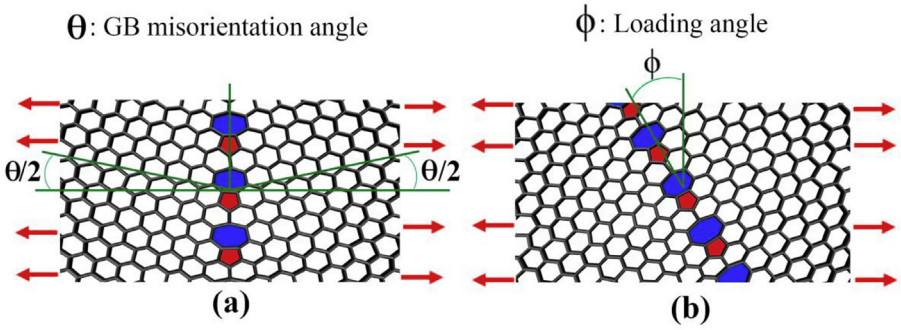

Fig. 1. A schematic of 2 grains showing a) GB misorientation angle (θ) and the b) tensile loading angle (ϕ). (A colour version of this figure can be viewed online.)

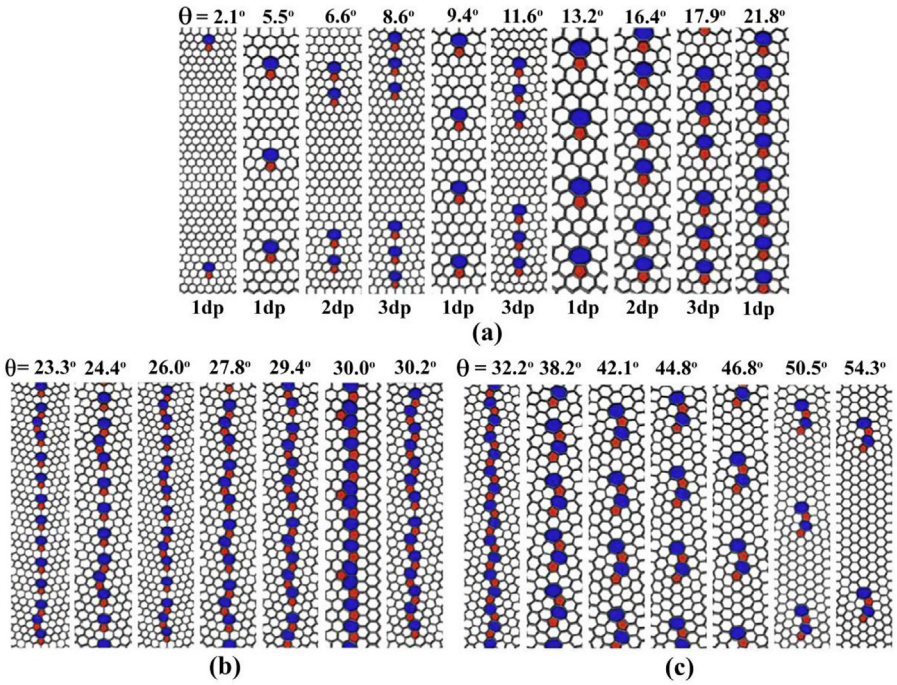

Fig. 2. The plots of possible tilt GB configurations (24 in total), showing (a) the armchair (AC) GBs with a misorientation angle (θ) ranging from 2.1° to 21.8°, (b) transition GBs with θ from 23.3° to 30.2° and (c) zigzag (ZZ) GBs with θ ranging from 32.2° to 54.3°. GB structures are modelled in clusters of pentagon (red) and heptagon (blue) membered rings as shown in each of the plots. (A colour version of this figure can be viewed online.)

where all their AC GBs were identical to ours and their GB strengths, where the loading angle was zero, are similar as well. Their ZZ GBs were different in that they did not contain any clustered 5|7|5|7 disclination dipoles. They also compared their ZZ GBs to ones that were constructed using CSL, which were identical to our ZZ GBs. Their ZZ GBs were energetically favorable to the CSL ZZ GBs and had slightly higher strength. However, they did not allow for out of plane buckling in the z direction in their calculations for energy, since they were trying to mimic the CVD process, where the sheets are constrained to grow on the substrates and remain flat. One study [17] used a trial and error method where they gradually deposited and removed atoms in the boundary of two patches of pristine sheets with prescribed grain misorientation and loading angle and then relaxed the structure. They iterated these steps until an energy minimum was reached. This leads to much different atomic arrangement of GB structures then ours shown in Fig. 2, but similar defect densities. Their studies only investigated the strength of the GBs when the tensile load was perpendicular to the GB, which they referred to as GB normal strength.

In order to calculate the stress-strain curves during deformation, the stress on each individual carbon atom was first calculated using the following equation [23].

$$\sigma_{ij}^{\alpha} = \frac{1}{\Omega^{\alpha}}\left[\frac{1}{2}m^{\alpha}v_i^{\alpha}v_j^{\alpha} + \sum_{\beta=1,n} r_{\alpha\beta}^{j} f_{\alpha\beta}^{i}\right] \quad (1)$$

where i and j denote the indices in the Cartesian coordinate system, α and β are the atomic indices, m^{α} and v^{α} are the mass and velocity of atom α, respectively, $r_{\alpha\beta}$ and $f_{\alpha\beta}$ are the distance and force between atoms α and β, respectively, and Ω^{α} is the atomic volume of atom α. The first term is the kinetic energy contribution and the second term is the pairwise energy contribution. The atomic volume is defined as

$$\Omega = \frac{l_0 \cdot w_0 \cdot t}{N} \quad (2)$$

where l_0 is the original length of the sheet, w_0 is the original width, t is the thickness which is assumed to be the interlayer spacing of graphene in graphite and is 3.35 Å, and N is the total number of atoms. Every 200 time steps the stress on each atom was computed and then the average stress over the entire sheet was used to obtain a spatial average.

The atomic stress induced by a disclination dipole can cause the corrugation of the graphene locally near the disclination dipole. As a result, GBs lead to out-of-the-plane fluctuation of the graphene sheet. As shown in Fig. 3, the overall out-of-the-plane fluctuation of the graphene sheet decreases as the defect density of the GB increases, which can be attributed to the mutual constraint of out-of-the-plane fluctuations between neighboring dipole defects.

When the graphene is stretched in the plane, it first straightens the out-of-the-plane fluctuations in the sheet. As shown in Fig. 4a, such a process results in negligible increase of tensile stress in the graphene. Once the graphene sheet is stretched taut, further elongation leads to increasing tensile stress until the final fracture of the sheet. Previous studies observed similar stress-strain behavior and shifted their curve to the left so that the initial flat segment of the stress-strain curves is not considered [54]. In this study we include all segments in the stress-strain curves and define the strain as $\frac{l-l_0}{l_0}$, where l is the current length of the deformed sheet and l_0 is the original length of the graphene sheet. Such a choice of strain definition is reasonable to more accurately capture the ductility of graphene with GBs (the tensile strain upon failure) as the straightening of the initial out-of-the-plane fluctuation does contribute to the deformability of graphene with GBs. However, it is worth to note that, the tensile strength of the graphene GB is nearly independent of the way the tensile strain is defined, as evident in Fig. 4.

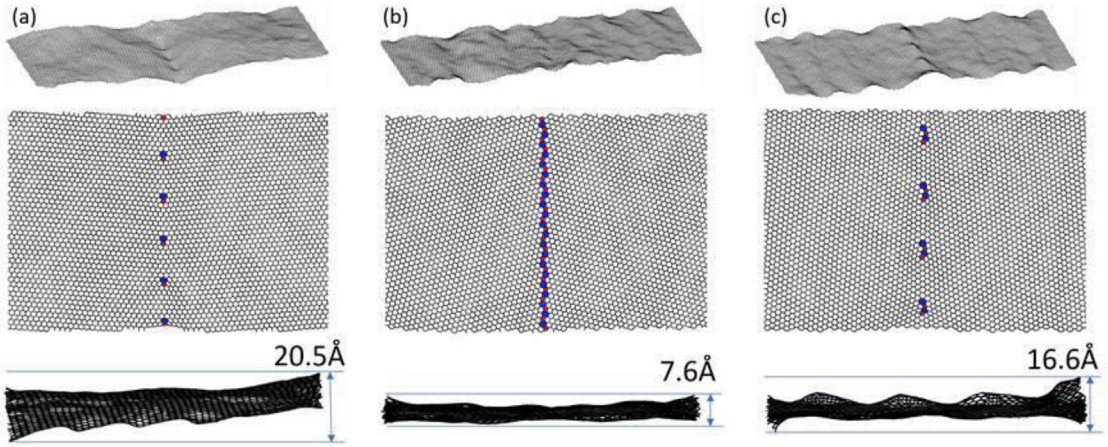

Fig. 3. Morphology of the graphene sheet with a tilt GB with (a) $\theta = 5.5°$, (b) $\theta = 32.2°$, (c) $\theta = 50.5°$. The top panel shows perspective view, the middle panel shows top view, and the bottom panel shows the side view of the graphene sheet. Note that the graphene sheet with higher defect density (b) has a relatively smaller out-of-the-plane fluctuation. (A colour version of this figure can be viewed online.)

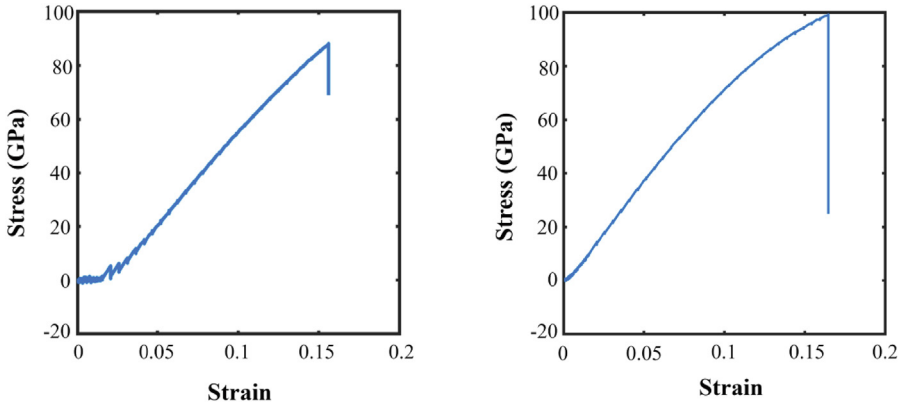

Fig. 4. Stress-strain curves for a graphene sheet with a GB with (a) $\theta = 5.5°$, which shows no significant increase in stress initially as the GB-induced out of the plane fluctuation in the graphene is pulled taut, and (b) $\theta = 32.2°$, which shows stress increasing as soon as the sheet is stretched, resulting from a rather flat initial morphology of the graphene sheet. Here the loading angle of 0° for both cases. (A colour version of this figure can be viewed online.)

Fig. 5a plots the stress-strain curves from representative simulation cases of graphene with a tilt GB subject to tension, in comparison with those of pristine graphene sheets of the same size subject to tension in the armchair and zigzag directions. The peak value of stress in each curve is defined as the tensile strength of that simulation case. Both tensile strength and failure strain of a graphene with a tilt GB are lower than those of a pristine graphene in either zigzag or armchair directions, a clear evidence of the effect of GB on mechanical properties of graphene.

Emerging from the comprehensive simulation studies of a graphene GB under arbitrary in-plane tension are three representative failure modes of the graphene, depending on the GB type and loading angle. For example, for an AC GB with a misorientation angle of 8.6° under a loading angle of 30°, it is shown that the failure initiates from the disclination dipoles, but then propagate in a direction roughly perpendicular to the tensile loading, resulting in the cracking of the graphene grain (Fig. 5b). Such a failure mode is termed as intragranular failure. For a ZZ GB with a misorientation angle of 46.8° under a loading angle of 10°, the failure initiates from the disclination dipoles along the GB, and then propagate along the GB. Such short cracks coalesce and form a long crack to fracture the graphene along the GB (Fig. 5c). Such a failure mode is termed as intergranular failure. For the same ZZ GB under a loading angle of 20°, it is shown that an intergranular crack is first formed, but it then deviates from the GB and propagates into the grain in a direction roughly perpendicular to the tension (Fig. 5d). Such a failure mode is termed transitional failure.

Fig. 6 plots a failure mode map of graphene GBs in the parameter space of GB misorientation angle and loading angle. Such a map delineates the holistic characteristics of the tensile failure of graphene GBs. These findings are crucial in understanding the failure behavior of polycrystalline graphene, but are missing from previous studies of graphene GBs in which only a tension perpendicular or parallel to the GB is considered ($\phi = 0°$, only intergranular failure occurs).

It is shown that for a GB with any misorientation angle, all three failure modes are possible, depending on the loading direction. Indeed, intergranular failure only occurs at a small range of loading angles (less than 10° for most GBs). All the fracture modes for the 0° loading angle are intergranular. As the loading angle increases the fracture mode changes to transitional and after 40° all fracture modes occur as intragranular cracking. The fracture mode is mainly transitional for the GB misorientation angles that have a high defect density up to the 40° loading angle. While the tensile failure always initiates from the bond breaking events at the disclination dipole so that the GB strength is dictated by the critical bond breaking (as to be further detailed in later sections), it is found that the initial bond breaking at the disclination dipole further develops and evolves

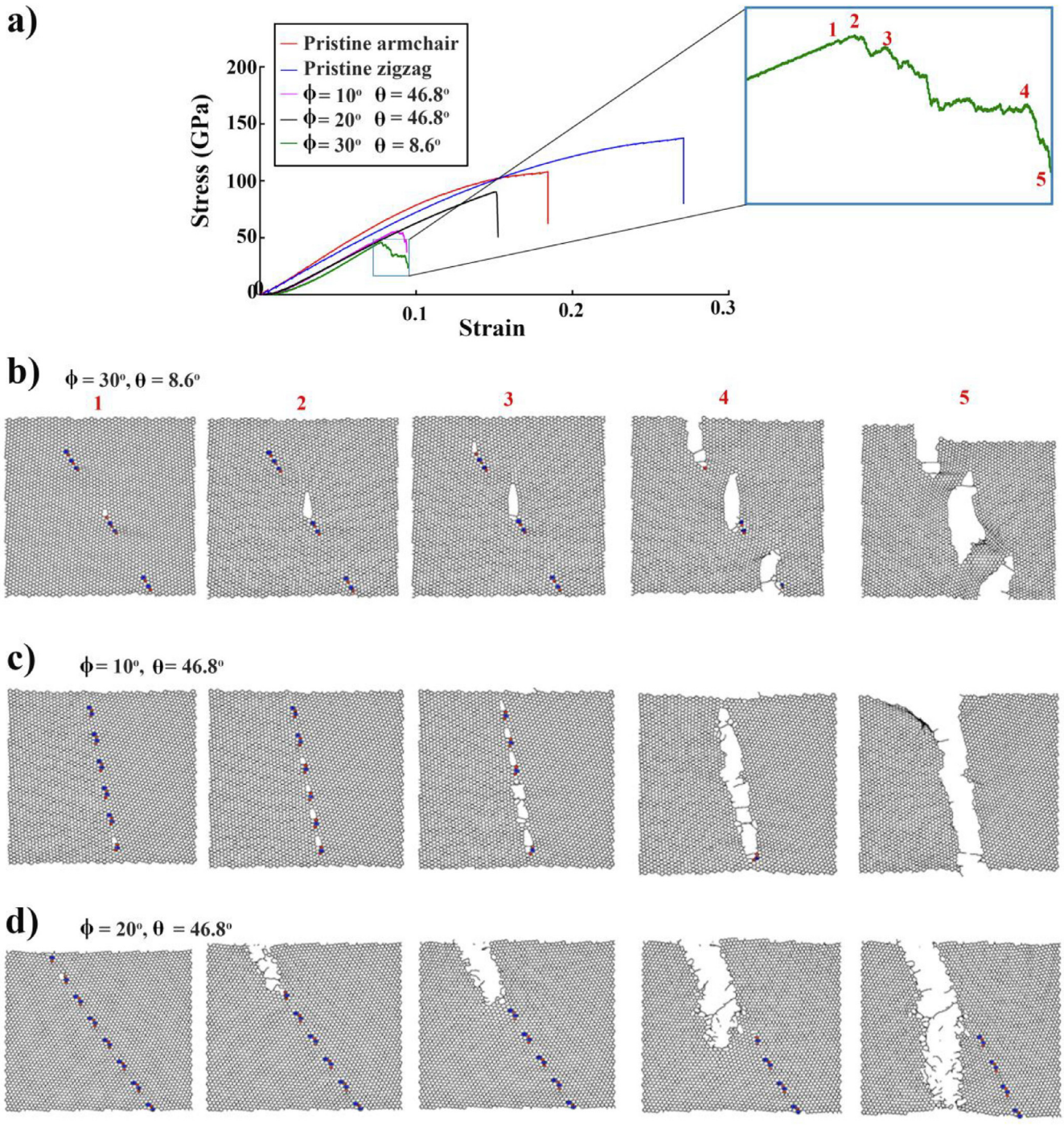

Fig. 5. (a) MD simulation results of stress-strain curves for representative cases of pristine as well as polycrystalline graphene under an in-plane tension. The tensile strength corresponds the peak stress in the curves. The simulation snapshots for three representative failure modes of GBs: (b) intragranular fracture ($\phi = 30^\circ$ and $\theta = 8.6^\circ$), (c) intergranular fracture ($\phi = 10^\circ$ and $\theta = 46.8^\circ$), (d) and transitional fracture ($\phi = 20^\circ$ and $\theta = 46.8^\circ$). (A colour version of this figure can be viewed online.)

into various failure modes of graphene GBs, governed by the interplay between the GB misorientation angle, loading angle as well as the orientation of the AC or ZZ directions in the graphene grains. For 0° loading angle, the GB is perpendicular to the loading direction and coincides with the direction with the maximum average tensile stress. As a result, the failure mode is always intergranular fracture, regardless of GB misorientation angle. When the loading angle is greater than 40°, the GB deviates substantially from the direction with the maximum average tensile stress (the direction perpendicular to tensile loading). Therefore, the initial bond breaking further propagates along the direction perpendicular to tensile loading, instead of further advancing along the GB. As a result, the failure mode is intragranular fracture. For intermediate loading angles, it is possible that the initial bond breaking first starts to further propagate along the GB, leads to intergranular cracks of finite size. Then such intergranular cracks deviate from GB and propagate along the direction perpendicular to tensile loading. As a result, the failure mode is transitional fracture. To further

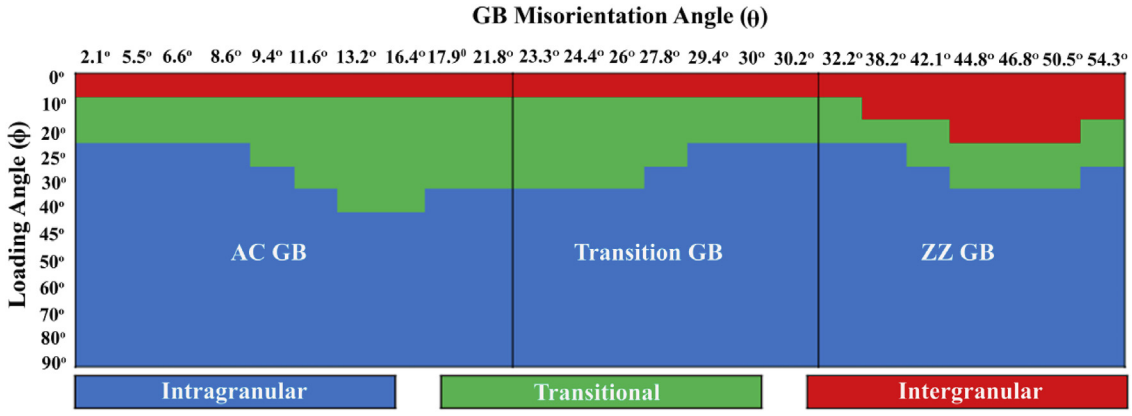

Fig. 6. A comprehensive failure mode map of polycrystalline graphene in the parameter space of GB misorientation angle (θ) and loading angle (ϕ). (A colour version of this figure can be viewed online.)

illustrate the interplay among the three key parameters that govern the failure mode, Fig. 7 plots two cases and their tensile failure modes. Both cases correspond to the same loading angle of $\phi = 40^\circ$. When the GB misorientation angle $\theta = 13.2^\circ$, it is shown that the ZZ direction of the bottom grain is about 4° away from the direction perpendicular to tensile loading. The initial bond breaking at the disclination dipoles first develop into a crack along the GB, then the two crack tips deviate from the GB and further propagate roughly perpendicular to the tensile direction, leading to a transitional fracture mode. While when the GB misorientation angle $\theta = 21.8^\circ$, the ZZ direction of the bottom grain coincides with the direction perpendicular to tensile loading. Recent studies have shown that for pristine graphene it is energetically favorable for failure to occur along its ZZ or AC directions [48]. As a result, instead of propagating along the GB, the initial bond breaking further develops into cracks perpendicular to the tensile loading, leading to an intragranular fracture mode.

Fig. 8 plots the failure strength of the GB as a function of loading angle, for all 24 GB configurations. For comparison, tensile strength of a pristine graphene sheet as a function of loading angle is also plotted in Fig. 8d. For AC GBs (Fig. 8a), the variations of failure strength against loading angle are significant and show a similar trend for all 10 AC GBs, with a minimum failure strength (as low as 53 GPa) always occurring at a loading angle of 30°. For transitional GBs, there is no common trend of variation of tensile strength against loading angle, but the overall level of failure strength is relatively high (about 100 GPa). For ZZ GBs, the lowest failure strength nearly always occurs at a 0° loading angle (except for the case of a GB with 32.2° misorientation angle).

When graphene was elongated parallel to the GB ($\phi = 90^\circ$) the strength of the sheets was all around 100 GPa, which is only slightly lower than pristine AC or ZZ graphene of around 120 GPa and 140 GPa, respectively. These results were always higher as compared to when they were pulled perpendicular to the GB ($\phi = 0^\circ$). This agrees with previous studies done on GBs [17,23,28,54,56,57,68]. Although the values of θ for the GBs in

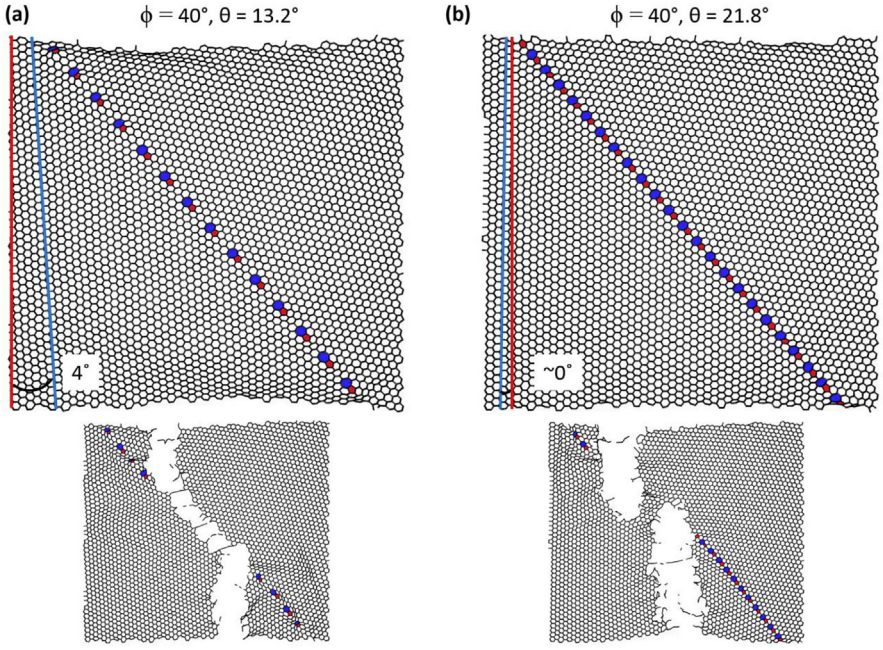

Fig. 7. (a) Intragranular fracture for $\phi = 40^\circ$, $\theta = 13.2^\circ$ (b) transitional fracture for $\phi = 40^\circ$, $\theta = 21.8^\circ$. Red line is the direction perpendicular to tensile loading, while the blue line is the ZZ direction of the bottom grain. (A colour version of this figure can be viewed online.)

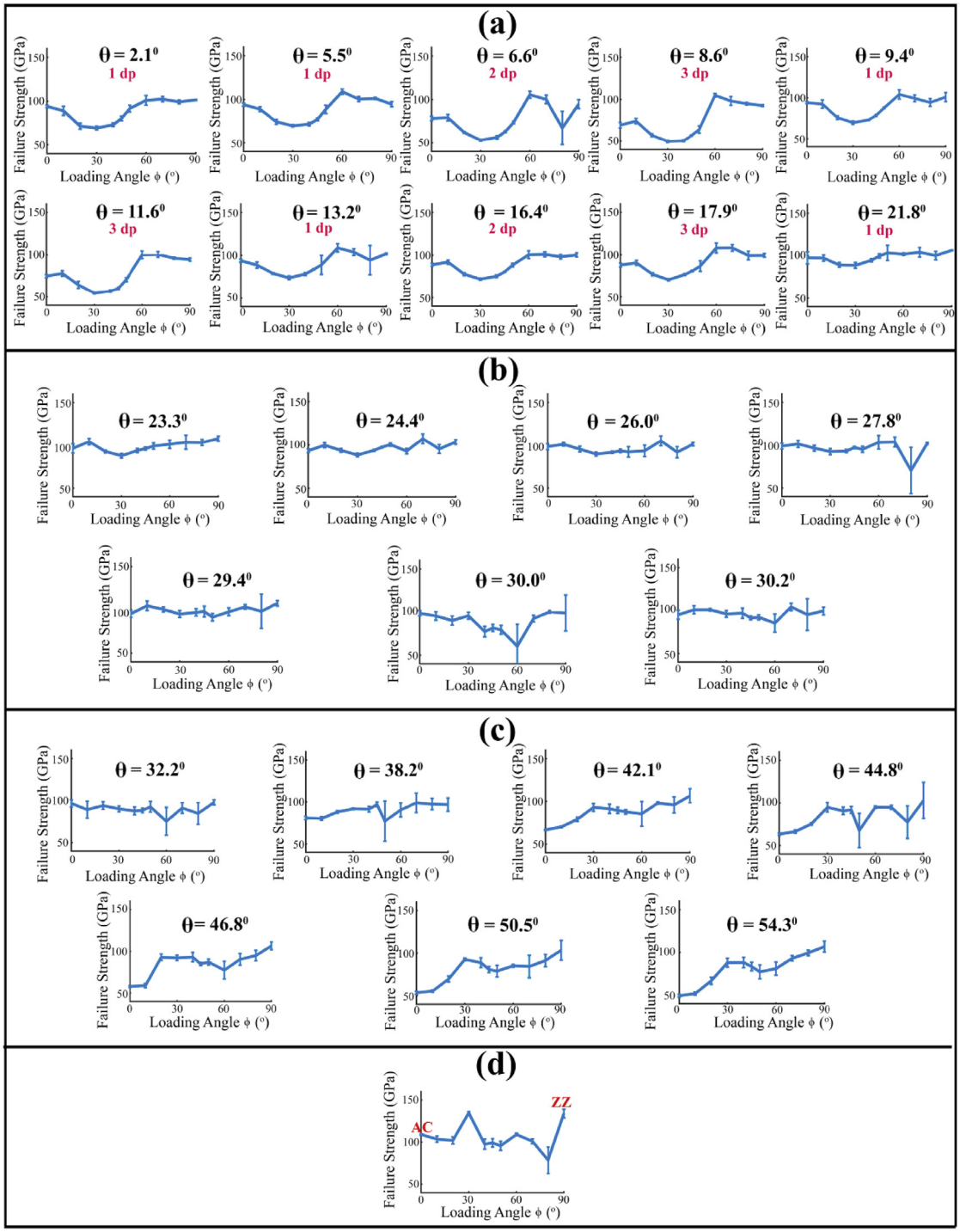

Fig. 8. The failure strength with errors bars for the standard deviation as a function of loading angle for 25 GB configurations. (a) AC GBs, (b) transition GBs, (c) ZZ GBs, and d) pristine (ZZ and AC) graphene. For AC GBs, failure strength is minimum for loading angle of 30° and for ZZ GBs, minimum strength always occurs near loading angle of 0° (except for the case of ZZ GB with $\theta = 32.2°$). Transition GBs show a higher failure strength (~100GPa) but depicts no trend of strength variation with respect to loading angle. "1dp", "2dp" and "3dp" in (a) indicate the number of dipoles present in the AC GBs. (A colour version of this figure can be viewed online.)

Refs. [17,28] are close to ours, the atomic arrangement of their atoms are quite different. However, the stress-strain response for each of these θ are similar with that in the present study. It is worth to note that when $\phi > 45°$, the GB spans the horizontal direction of the simulation model, but not the vertical direction (perpendicular to tensile loading direction). It is found that the predicted failure strength from such a simulation model agrees with that from a longer simulation model in which the GB spans the vertical direction. Therefore, results from the parametric study using the 120 Å × 120 Å graphene sheets can reasonably capture the nature of the GB tensile strength in graphene.

The MD simulations capture the atomistic scale deformation signatures that govern the failure behaviors of the graphene GBs, which in turn help understand the origin of the variations of failure

strength against loading angle shown in Fig. 8. We find that the graphene fracture initiates from bond breaking at the disclination dipole [69], followed by the coalescence of such defects due to bond breaking into a long crack, whose further propagation leads to the failure of the graphene. In other words, the failure strength of the GB is governed by the bond breaking at the disclination dipole. This can be further understood as follows. In a pristine graphene, without external loading in its plane, the carbon-carbon (C–C) bonds are rather relaxed and stress-free. By contrast, a disclination dipole in graphene causes distortion of graphene crystal lattice and thus can generate an intrinsic stress field in the graphene, even if there is no external loading. Such an intrinsic stress field decays with distance from the disclination dipole. Therefore, the resulting intrinsic stress field due to a GB in graphene can be computed by superimposing the intrinsic stress field due to individual disclination dipoles along the GB (as to be discussed in detailed in Section 4). When the graphene is subject to external tensile loading, the C–C bond with the highest intrinsic tensile stress fails first and initiates the failure process.

Fig. 9 plots one of the disclination dipoles along an AC GB under tension. The C–C bond with the highest tensile stress is in the heptagon of the disclination dipole (highlighted by a red line segment in Fig. 9a).

Simulation clearly shows that the breaking of this bond opens a void (Fig. 9b) in graphene, which further propagates and leads to the failure of the whole graphene (Fig. 9b), which validates the failure mechanism described above. As shown in Fig. 9c, when the loading angle of an AC GB is about 30°, the C–C bond with the highest intrinsic tensile stress is oriented almost along the tensile loading direction and breaks first under tension (Fig. 9d). The external tensile stress required to break this bond is the lowest when the loading angle is about 30°. Since all AC GBs are made of arrays of disclination dipoles, the failure strength of such GBs becomes the lowest under a loading angle of about 30°, as shown in Fig. 8a.

Fig. 10a plots a double disclination dipole in a ZZ GB. Fig. 10b plots the intrinsic stress field due to the double disclination dipole, showing that the highest tensile stress occurs in the horizontal C–C bond in the end heptagon. Upon a tensile loading perpendicular to the ZZ GB ($\phi = 0°$), the stress in that bond further increases (Fig. 10c) until the bond is broken, resulting in an opening that further propagates to fracture the graphene (Fig. 10d). This also explains for most ZZ GBs, the lowest failure strength corresponds to the loading angle of 0°, as shown in Fig. 5c. In the curves for all ZZ GBs shown in Fig. 9c, it also shows that there exists a local minimum of failure strength at a loading angle of about 50°. This can be clarified by Fig. 10e–h. At a 50° loading angle, the C–C bond next to that with highest intrinsic tensile stress aligns approximately in parallel to the tensile loading direction (Fig. 10e and f). Upon a tensile loading, the tensile stress in this bond becomes the highest (Fig. 10g), which eventually causes the bond breaking and further leads to the failure of the graphene (Fig. 10h).

4. A continuum mechanics model of the strength of AC and ZZ GBs of graphene

MD simulations reveal that the failure strength of graphene GBs is governed by the breaking of the C–C bond with the highest intrinsic tensile stress (termed as the critical C–C bond), as labeled in Figs. 9a and 10a. A continuum mechanics model based on disclination dipole induced stress field can be developed to better understand the dependence of failure strength of AC and ZZ GBs on GB misorientation angle. The sheets initially buckle out of plane and the continuum model is based off flat 2D sheets [27], but the equations still apply because during the tensile tests the sheets are pulled flat.

Consider an AC GB made of an array of disclination dipoles [69], as illustrated in Fig. 11a. For the ith disclination dipole with the center of its pentagon at $A(x_A^i, y_A^i)$ and the center of its heptagon at $B(x_B^i, y_B^i)$, the induced stress field in the graphene at (x, y) is given by:

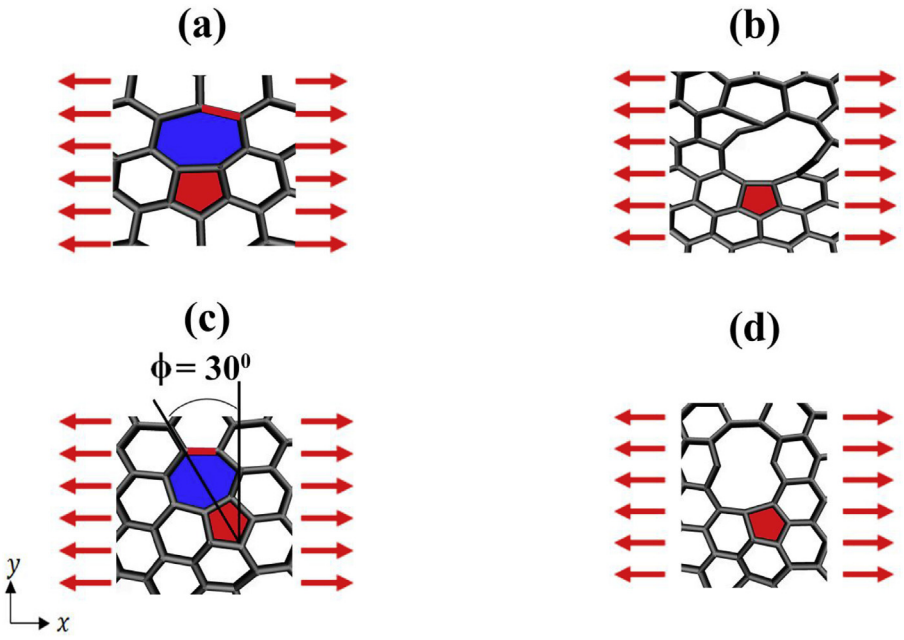

Fig. 9. (a) For an AC GB, the C-C bond with the highest intrinsic tensile stress is in the heptagon of the disclination dipole (highlighted by a red line segment). Under a tensile load with $\phi = 0°$, this bond breaks first, opening a void in graphene (b), which further propagates and leads to the failure of the whole graphene. (c) when the loading angle $\phi = 30°$, the critical bond (red) aligns almost parallel to the loading direction and (d) breaks first due to the highest initial stress. This explains the strength of AC GBs at a loading angle $\phi = 30°$ is always the lowest. (A colour version of this figure can be viewed online.)

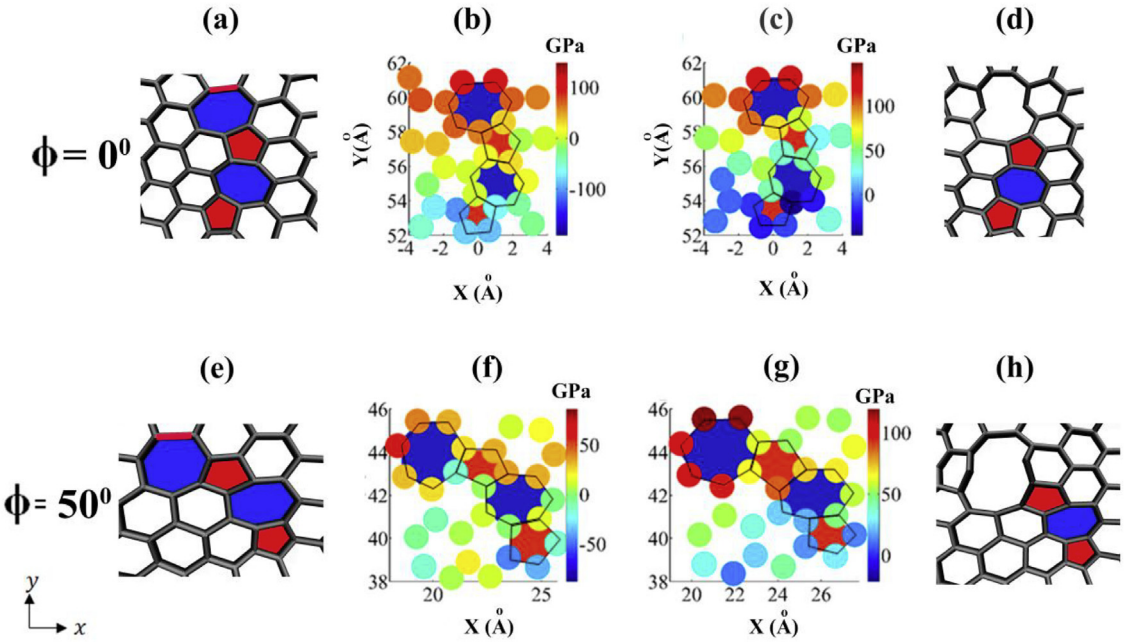

Fig. 10. (a) For a ZZ GB the highest intrinsic tensile stress occurs in the horizontal C-C bond in the top heptagon of the double disclination dipole (highlighted by a red line segment). (b) The colored solid circles depict the level of intrinsic stress for each atom. (c) Under an applied tensile load with $\phi = 0°$, the stress level further increases. (d) The breaking of the critical C-C bond opens a void and initiates the failure process of the graphene. This explains why the lowest failure strength for most ZZ GBs is at $\phi = 0°$. (e) When $\phi = 50°$, the critical C-C bond aligns approximately parallel to the tensile loading direction (highlighted in red). (f) Stresses in each atom before loading. (g) Upon loading, the tensile stress in this bond becomes the highest, (h) which eventually causes the bond breaking and further leads to the failure of the graphene. This explains the local minimum at $\phi = 50°$ in Fig. 5(c) for ZZ GBs. (A colour version of this figure can be viewed online.)

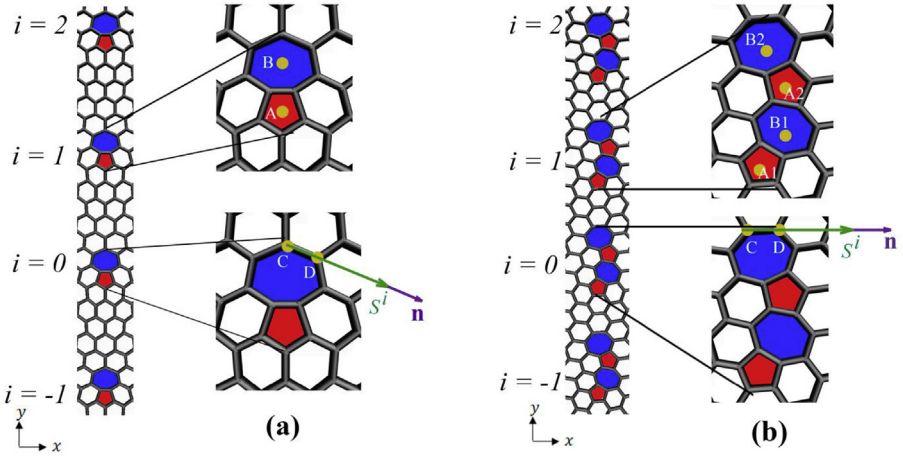

Fig. 11. The AC GB (a) is made of an array of periodic pentagon-heptagon disclination dipoles. In (a), A and B indicate the center of the heptagon and pentagon of the ith disclination dipole. S^i is the intrinsic stress at i = 0 due to the ith dipole and **n** is the unit vector defining the direction of the critical bond. (b) shows the corresponding schematic for a ZZ GB made of a periodic array of pentagon-heptagon-pentagon-heptagon dipole clusters. (A colour version of this figure can be viewed online.)

$$\boldsymbol{\sigma}^i = \begin{bmatrix} \sigma^i_{xx} & \sigma^i_{xy} \\ \sigma^i_{xy} & \sigma^i_{yy} \end{bmatrix} \tag{3}$$

where

$$\sigma^i_{xx} = \frac{E}{12}\left[ln\left(\frac{r^i_A}{r^i_B}\right) + \frac{(y-y^i_A)^2}{(r^i_A)^2} - \frac{(y-y^i_B)^2}{(r^i_B)^2}\right] \tag{4}$$

$$\sigma^i_{yy} = \frac{E}{12}\left[ln\left(\frac{r^i_A}{r^i_B}\right) + \frac{(x-x^i_A)^2}{(r^i_A)^2} - \frac{(x-x^i_B)^2}{(r^i_B)^2}\right] \tag{5}$$

$$\sigma^i_{xy} = \frac{E}{12}\left[ln\left(\frac{r^i_A}{r^i_B}\right) + \frac{(x-x^i_A)(y-y^i_A)}{(r^i_A)^2} - \frac{(x-x^i_B)(y-y^i_B)}{(r^i_B)^2}\right] \tag{6}$$

E is the Young's Modulus of graphene, and $r^i_A = \sqrt{(x-x^i_A)^2 + (y-y^i_A)^2}$, $r^i_B = \sqrt{(x-x^i_B)^2 + (y-y^i_B)^2}$.

Denote the directional unit vector of the critical C–C bond in the

0^{th} disclination dipole as $\mathbf{n} = \begin{bmatrix} n_x \\ n_y \end{bmatrix}$. The intrinsic tensile stress in the critical C–C bond at $i = 0$ due to the ith disclination dipole is given by

$$S^i = \left(\boldsymbol{\sigma}^i \cdot \mathbf{n}\right)\mathbf{n} \tag{7}$$

Therefore, the failure strength of the AC GB can be given by

$$\sigma_T = \sigma_0 - \sum_{i=\pm 1}^{i=\pm\infty} S^i \tag{8}$$

where σ_0 is a fitting parameter used to fit the calculations to the MD results and is the strength of the critical C–C bond at $i = 0$ without the influence of other disclination dipoles, and the summation $\sum_{i=\pm 1}^{i=\pm\infty}$ S^i represents the combined effect on the GB strength from all other disclination dipoles.

The above consideration can also be carried out for a ZZ GB made of a periodic array of pentagon-heptagon-pentagon-heptagon disclination clusters as illustrated in Fig. 11b.

For the ith pentagon-heptagon-pentagon-heptagon disclination cluster with the centers of its pentagons at *A1* (x^i_{A1}, y^i_{A1}) and *A2* (x^i_{A2}, y^i_{A2}) and the center of its heptagons at *B1* (x^i_{B1}, y^i_{B1}) and *B2* (x^i_{B2}, y^i_{B2}), the induced stress field [17,70,71] in the graphene at (x, y) is given by:

$$\boldsymbol{\sigma}^i = \begin{bmatrix} \sigma^i_{xx} & \sigma^i_{xy} \\ \sigma^i_{xy} & \sigma^i_{yy} \end{bmatrix} \tag{9}$$

where

$$\sigma^i_{xx} = \frac{E}{12}\left[ln\left(\frac{r^i_{A1}}{r^i_{B1}}\right) + \frac{(y - y^i_{A1})^2}{(r^i_{A1})^2} - \frac{(y - y^i_{B1})^2}{(r^i_{B1})^2}\right] + \frac{E}{12}\left[ln\left(\frac{r^i_{A2}}{r^i_{B2}}\right) + \frac{(y - y^i_{A2})^2}{(r^i_{A2})^2} - \frac{(y - y^i_{B2})^2}{(r^i_{B2})^2}\right] \tag{10}$$

$$\sigma^i_{yy} = \frac{E}{12}\left[ln\left(\frac{r^i_{A1}}{r^i_{B1}}\right) + \frac{(x - x^i_{A1})^2}{(r^i_{A1})^2} - \frac{(x - x^i_{B1})^2}{(r^i_{B1})^2}\right] + \frac{E}{12}\left[ln\left(\frac{r^i_{A2}}{r^i_{B2}}\right) + \frac{(x - x^i_{A2})^2}{(r^i_{A2})^2} - \frac{(x - x^i_{B2})^2}{(r^i_{B2})^2}\right] \tag{11}$$

$$\sigma^i_{xy} = \frac{E}{12}\left[ln\left(\frac{r^i_{A1}}{r^i_{B1}}\right) + \frac{(x - x^i_{A1})(y - y^i_{A1})}{(r^i_{A1})^2} - \frac{(x - x^i_{B1})(y - y^i_{B1})}{(r^i_{B1})^2}\right] + \frac{E}{12}\left[ln\left(\frac{r^i_{A2}}{r^i_{B2}}\right) + \frac{(x - x^i_{A2})(y - y^i_{A2})}{(r^i_{A2})^2} - \frac{(x - x^i_{B2})(y - y^i_{B2})}{(r^i_{B2})^2}\right] \tag{12}$$

$$\text{and} \cdot r^i_{A1} = \sqrt{(x - x^i_{A1})^2 + (y - y^i_{A1})^2}, r^i_{B1} = \sqrt{(x - x^i_{B1})^2 + (y - y^i_{B1})^2} \text{and} \cdot r^i_{A2}\sqrt{(x - x^i_{A2})^2 + (y - y^i_{A2})^2} \cdot r^i_{B2}\sqrt{(x - x^i_{B2})^2 + (y - y^i_{B2})^2} \tag{13}$$

Denote the directional unit vector of the critical C–C bond in the 0^{th} pentagon-heptagon-pentagon-heptagon disclination cluster as $\mathbf{n} = \begin{bmatrix} n_x \\ n_y \end{bmatrix}$. The intrinsic tensile stress in the critical C–C bond at $i = 0$ due to the ith disclination dipole is given by

$$S^i = \left(\boldsymbol{\sigma}^i \cdot \mathbf{n}\right) \cdot \mathbf{n}, \tag{14}$$

where $\mathbf{n}$ is the directional unit vector of the critical C–C bond.

Therefore, the failure strength of the ZZ GB can be given by

$$\sigma_T = \sigma_0 - \sum_{i=\pm 1}^{i=\pm\infty} S^i \tag{15}$$

where σ_0 is a fitting parameter used to fit the calculations to the MD results and is the strength of the critical C–C bond at $i = 0$ without the influence of other pentagon-heptagon-pentagon-heptagon disclination clusters, and the summation $\sum_{i=\pm 1}^{i=\pm\infty} S^i$ represents the combined effect on the GB strength from all other pentagon-heptagon-pentagon-heptagon disclination clusters.

In a recent study [27], a similar disclination dipole based continuum mechanics model was used to predict the strength of graphene GB for the case of loading angle of $\phi = 0°$. In that study, only the contribution of σ^i_{xx} in the disclination dipole induced stress tensor (Eq. (3)) to the critical bond strength is considered. As to be shown in Section 5, such an approximation leads to a predicted GB strength with modest but acceptable difference from the results from MD simulations, for the case of loading angle of $\phi = 0°$. By contrast, the predicted GB strength from the present model considering the contribution of all components in the disclination dipole induced stress tensor agrees well with MD simulations. Furthermore, for the cases of non-zero loading angles (especially larger loading angles), the previous model with approximation would not be able to predict the GB strength accurately, however, the prediction from the present model agrees fairly well with MD simulation results.

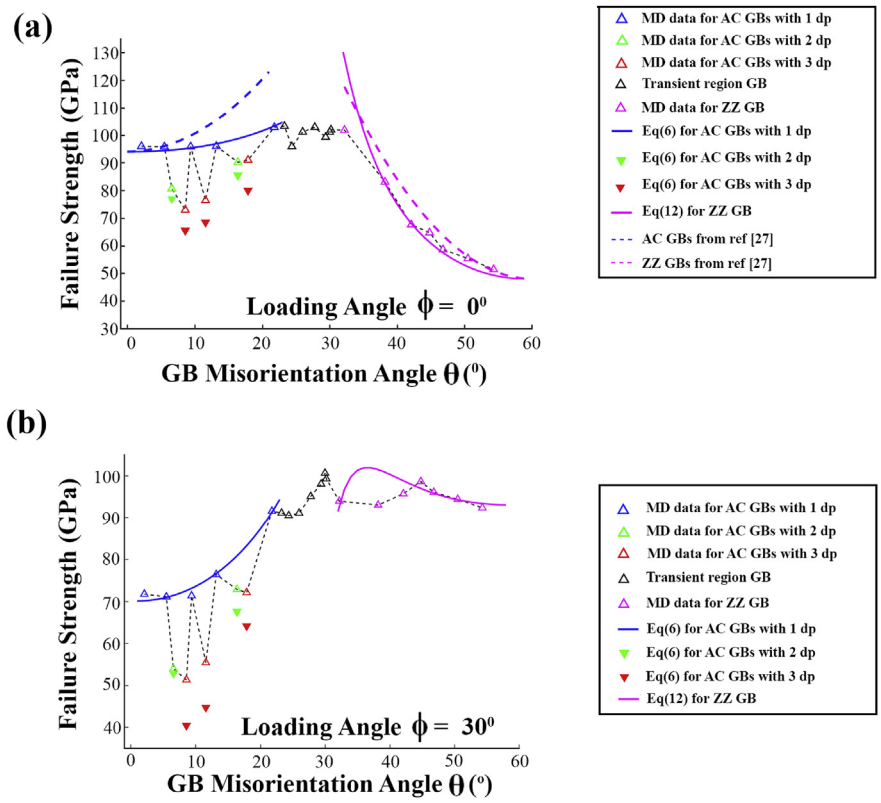

Fig. 12. The GB failure strength as a function of GB misorientation angle for (a) 0° loading angle, and (b) 30° loading angle. Hollow symbols denote results from MD simulations. The prediction from the continuum mechanics model (Eqs. (8) and (14)) are shown in solid curve (with 1dp) and solid symbols (2dp and 3dp). In (a), it is evident that predictions from Eqs. (8) and (14) agree well with the MD results (1dp). Here $\sigma_0 = 94$ GPa. For comparison, the predictions from Ref. [27] (dashed curves) show a modest difference from the MD results. In (b), it is shown that the continuum model can still give a reasonable prediction of the failure strength of both AC and ZZ GBs, when compared with the MD results. Here, for 30° loading angle of AC GBs, $\sigma_0 = 68$ GPa. (A colour version of this figure can be viewed online.)

5. Discussions

Fig. 12 plots failure strength of graphene GB as a function of GB misorientation angle, for the case of (a) 0° loading angle and (b) 30° loading angle. For the 0° loading angle the results agree very well with tensile tests on sheets with GBs that have similar misorientation angles in previous studies [17,23,24,27,28,54]. When $\phi = 0°$, it is shown that for AC GBs made of an array of evenly distributed pentagon-heptagon dipoles (1dp) and ZZ GBs, the GB strengths predicted by the continuum mechanics model presented in Section 4 (Eq. (8) for AC GBs and Eq. (14) for ZZ GBs) agree well with the prediction from the molecular dynamic simulations. For $\phi = 0°$, σ_0 is about 94 GPa for AC GBs and about 51 GPa for ZZ GBs. The strength of AC GBs made of an arrays of dipole clusters (2dp and 3dp) is generally lower that of 1dp AC GBs. This can be understood that, 2dp or 3dp leads to an elevated intrinsic tensile stress to the critical C—C bond due to the smaller spacing between the dipoles in the dipole clusters, as evident from Fig. 1. In general, the GB strength increases with increasing GB misorientation angle θ for AC GBs and with decreasing GB misorientation angle θ for ZZ GBs. The GB strength is more sensitive to θ for ZZ GBs than for AC GBs. These trends agree with results from recent studies. Moreover, it is shown that the present continuum model agrees better with results from molecular dynamics simulation than the previous approximate model [27] shown with dashed lines in Fig. 12, since all in plane stress components, σ_{xx}, σ_{yy}, and σ_{xy}, are included in our model.

When $\phi = 30°$, it is shown that the general dependence of GB strength on GB misorientation angle is similar to that when $\phi = 0°$ (Fig. 12b). The major difference is that, the GB strength becomes more sensitive to θ for AC GBs, but much less sensitive to θ for ZZ GBs. Also, it is shown that the present continuum mechanics model can predict the GB strength is in good agreement with molecular dynamics simulations, which is otherwise not possible using the previous approximate model.

Fig. 13 plots the contour of the strength (a) and the failure strain (b) of graphene tilt GB in the parameter space of GB misorientation angle θ and loading angle ϕ. This figure, together with Fig. 4, summarizes the holistic characteristics of the tensile failure of graphene tilt GBs.

6. Conclusions

Pristine graphene has a failure strength as high as 130 GPa, but when defects are present in graphene, its failure strength can be significantly reduced, e.g., as low as 50 GPa with a tilt GB defect. The polycrystalline nature of commonly used large area graphene grown via CVD requires a better understanding of the deformation and failure behavior of graphene GBs in arbitrary in-plane tension, which is lacking from existing studies. Through a comprehensive study using molecular dynamics simulations and a continuum mechanics model, we report the dependence of failure strength of graphene GBs on both GB misorientation angle and loading angle in their full spectrum. The systematic molecular dynamics simulation study also reveals three different failure modes of graphene GBs, depending on GB misorientation angle and loading angle. In real polycrystalline graphene samples, the GBs could vary from the ideal tilt GBs (e.g., slightly more tortuous than a straight tilt GB). Nonetheless, the holistic characteristics of the tensile failure of graphene

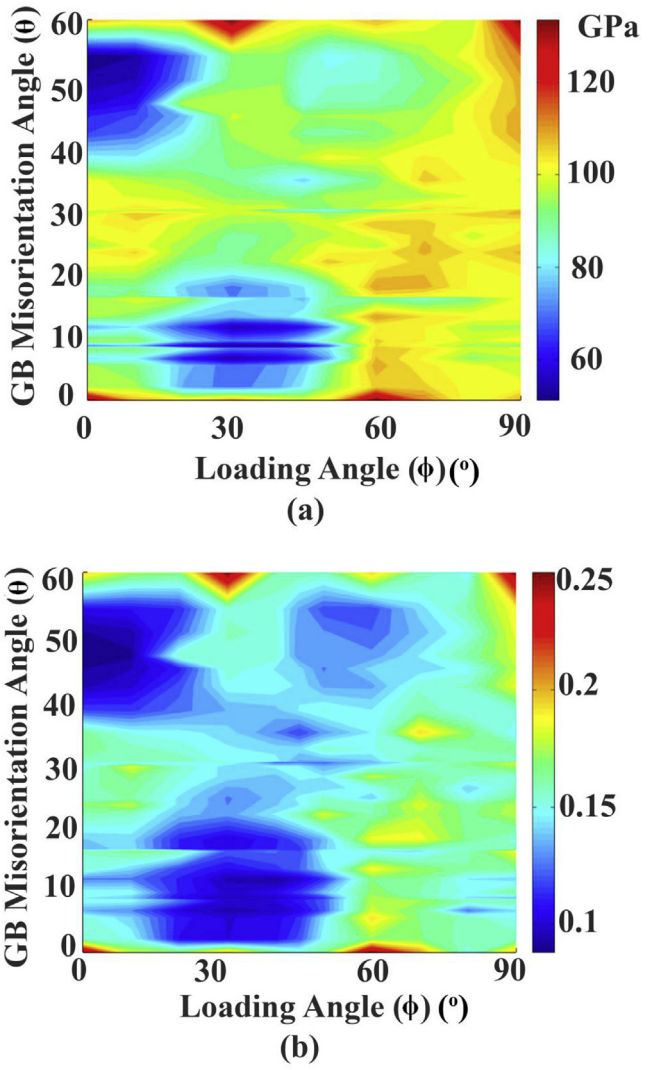

Fig. 13. The contour plots of (a) failure strength and (b) failure strain of graphene GBs in the parameter space of loading angle and GB misorientation angle. (A colour version of this figure can be viewed online.)

GBs from the present study could offer important insight on a better understanding of the mechanical response of graphene GBs in real samples under loads, and also shed light on understanding the GBs in other two-dimensional materials.

Acknowledgement

The authors acknowledge the support from the NASA National Institute of Aerospace Langley Professor Program. The authors acknowledge the University of Maryland supercomputing resources (http://hpcc.umd.edu) made available for conducting the research reported in this paper.

References

[1] D. Akinwande, C.J. Brennan, J.S. Bunch, P. Egberts, J.R. Felts, H. Gao, R. Huang, J.S. Kim, T. Li, Y. Li, K.M. Liechti, N. Lu, H.S. Park, E.J. Reed, P. Wang, B.I. Yakobson, T. Zhang, Y.W. Zhang, Y. Zhou, Y. Zhu, A review on mechanics and mechanical properties of 2D materials—graphene and beyond, Extrem. Mech. Lett. 13 (2017) 42–77.

[2] A. Kaplan, Z. Yuan, J.D. Benck, A. Govind Rajan, X.S. Chu, Q.H. Wang, M.S. Strano, Current and future directions in electron transfer chemistry of graphene, Chem. Soc. Rev. 46 (2017) 4530–4571.

[3] B.C. Janegitz, T.A. Silva, A. Wong, L. Ribovski, F.C. Vicentini, M.D.P. Taboada Sotomayor, O. Fatibello-Filho, The application of graphene for in vitro and in vivo electrochemical biosensing, Biosens. Bioelectron. 89 (2017) 224–233.

[4] C. Zhu, T. Liu, F. Qian, T.Y.J. Han, E.B. Duoss, J.D. Kuntz, C.M. Spadaccini, M.A. Worsley, Y. Li, Supercapacitors based on three-dimensional hierarchical graphene aerogels with periodic macropores, Nano Lett. 16 (2016) 3448–3456.

[5] J.Y. Lee, J.H. Lee, M.J. Kim, J.K. Dash, C.H. Lee, R. Joshi, S. Lee, J. Hone, A. Soon, G.H. Lee, Direct observation of grain boundaries in chemical vapor deposited graphene, Carbon 115 (2017) 147–153.

[6] D.W. Shin, D. Sung, J.S. Hong, M. Kim, S.S. Yoon, Y.J. Song, G. Kim, S. Hong, J.B. Yoo, Observation of graphene grain boundaries through selective adsorption of rhodamine B using fluorescence microscopy, Carbon 108 (2016) 72–78.

[7] X. Li, W. Cai, J. An, S. Kim, J. Nah, D. Yang, R. Piner, A. Velamakanni, I. Jung, E. Tutuc, S.K. Banerjee, L. Colombo, R.S. Ruoff, Large-area synthesis of high-quality and uniform graphene films on copper foils, Science 324 (2009) 1312–1314.

[8] A. Reina, X.T. Jia, J. Ho, D. Nezich, H.B. Son, V. Bulovic, M.S. Dresselhaus, J. Kong, Large area, few-layer graphene films on arbitrary substrates by chemical vapor deposition, Nano Lett. 9 (2009) 30–35.

[9] O. V Yazyev, Y.P. Chen, Polycrystalline graphene and other two-dimensional materials, Nat. Nanotechnol. 9 (2014) 755–767.

[10] T.H. Liu, G. Gajewski, C.W. Pao, C.C. Chang, Structure, energy, and structural transformations of graphene grain boundaries from atomistic simulations, Carbon 49 (2011) 2306–2317.

[11] Y. Liu, B.I. Yakobson, Cones, pringles, and grain boundary landscapes in graphene topology, Nano Lett. 10 (2010) 2178–2183.

[12] H. Yu, N. Gupta, Z. Hu, K. Wang, B.R. Srijanto, K. Xiao, D.B. Geohegan, B.I. Yakobson, Tilt grain boundary topology induced by substrate topography, ACS Nano 11 (2017) 8612–8618.

[13] Z. Zhang, Y. Yang, F. Xu, L. Wang, B.I. Yakobson, Unraveling the sinuous grain boundaries in graphene, Adv. Funct. Mater. 25 (2015) 367–373. http://doi.wiley.com/10.1002/adfm.201403024.

[14] M. Chen, S. Quek, Z. Sha, C. Chiu, Q. Pei, Y. Zhang, Effects of grain size, temperature and strain rate on the mechanical properties of polycrystalline graphene – a molecular dynamics study, Carbon 85 (2015) 135–146.

[15] Y. Li, A. Wei, H. Ye, H. Yao, Mechanical and thermal properties of grain boundary in planar heterostructure of graphene and hexagonal boron nitride, Nanoscale (2017) 3497–3508.

[16] B. Mortazavi, G. Cuniberti, Atomistic modeling of mechanical properties of polycrystalline graphene, Nanotechnology 25 (2014).

[17] J. Wu, Y. Wei, Grain misorientation and grain-boundary rotation dependent mechanical properties in polycrystalline graphene, J. Mech. Phys. Solid. 61 (2013) 1421–1432.

[18] A. Bagri, S.P. Kim, R.S. Ruoff, V.B. Shenoy, Thermal transport across twin grain boundaries in polycrystalline graphene from nonequilibrium molecular dynamics simulations, Nano Lett. 11 (2011) 3917–3921.

[19] K. Azizi, P. Hirvonen, Z. Fan, A. Harju, K.R. Elder, T. Ala-Nissila, S.M.V. Allaei, Kapitza thermal resistance across individual grain boundaries in graphene, Carbon 125 (2017) 384–390.

[20] A.W. Tsen, L. Brown, M.P. Levendorf, F. Ghahari, P.Y. Huang, R.W. Havener, C.S. Ruiz-Vargas, D.A. Muller, P. Kim, J. Park, Tailoring electrical transport across grain boundaries in polycrystalline graphene, Science 336 (2012) 1143–1146.

[21] H. Zhang, G. Lee, C. Gong, L. Colombo, K. Cho, Grain boundary effect on electrical transport properties of graphene, J. Phys. Chem. C 118 (2014) 2338–2343.

[22] T. Ma, Z. Liu, J. Wen, Y. Gao, X. Ren, H. Chen, C. Jin, X.L. Ma, N. Xu, H.M. Cheng, W. Ren, Tailoring the thermal and electrical transport properties of graphene films by grain size engineering, Nat. Commun. 8 (2017) 1–9.

[23] R. Grantab, V.B. Shenoy, R.S. Ruoff, Anomalous strength characteristics of tilt grain boundaries in graphene, Science 330 (2010) 946–948.

[24] T. Liu, C.W. Pao, C. Chang, Effects of dislocation densities and distributions on graphene grain boundary failure strengths from atomistic simulations, Carbon 50 (2012) 3465–3472.

[25] J. Xu, G. Yuan, Q. Zhu, J. Wang, S. Tang, L. Gao, Enhancing strength of graphene by denser grain boundary, ACS Nano 12 (2018) 4529–4535.

[26] B. Yang, S. Wang, Y. Guo, J. Yuan, Y. Si, S. Zhang, H. Chen, Strength and failure behavior of a graphene sheet containing bi-grain-boundaries, RSC Adv. 4 (2014) 54677–54683.

[27] Y. Wei, J. Wu, H. Yin, X. Shi, R. Yang, M. Dresselhaus, The nature of strength enhancement and weakening by pentagon–heptagon defects in graphene, Nat. Mater. 11 (2012) 759–763.

[28] J. Han, S. Ryu, D. Sohn, S. Im, Mechanical strength characteristics of asymmetric tilt grain boundaries in graphene, Carbon 68 (2014) 250–257.

[29] Y.I. Jhon, P.S. Chung, R. Smith, K.S. Min, G.Y. Yeom, M.S. Jhon, Grain boundaries orientation effects on tensile mechanics of polycrystalline graphene, RSC Adv. 3 (2013) 9897.

[30] B. Yang, S. Wang, Y. Guo, J. Yuan, Y. Si, S. Zhang, H. Chen, Strength and failure behavior of a graphene sheet containing bi-grain-boundaries, RSC Adv. 4 (2014) 54677–54683.

[31] H. Zhang, Z. Duan, X. Zhang, C. Liu, J. Zhang, J. Zhao, Strength and fracture behavior of graphene grain boundaries: effects of temperature, inflection, and symmetry from molecular dynamics, Phys. Chem. Chem. Phys. 15 (2013)

11794–11799.
[32] I.A. Ovid'ko, A.G. Sheinerman, Cracks at disclinated grain boundaries in graphene, J. Phys. D Appl. Phys. 46 (2013) 345305.
[33] T. Zhang, X. Li, H. Gao, Designing graphene structures with controlled distributions of topological defects: a case study of toughness enhancement in graphene ruga, Extrem. Mech. Lett. 1 (2014) 3–8.
[34] Z.D. Sha, Q.X. Pei, Z.S. Liu, V.B. Shenoy, Y.W. Zhang, Is the failure of large-area polycrystalline graphene notch sensitive or insensitive? Carbon 72 (2014) 200–206.
[35] Z. Song, V.I. Artyukhov, B.I. Yakobson, Z. Xu, Pseudo Hall-Petch strength reduction in polycrystalline graphene, Nano Lett. 13 (2013) 1829–1833.
[36] L. Yi, Z. Yin, Y. Zhang, T. Chang, A theoretical evaluation of the temperature and strain-rate dependent fracture strength of tilt grain boundaries in graphene, Carbon 51 (2013) 373–380.
[37] T. Zhang, X. Li, S. Kadkhodaei, H. Gao, Flaw insensitive fracture in nanocrystalline graphene, Nano Lett. 12 (2012) 4605–4610.
[38] J. Zhang, J. Zhao, J. Lu, Intrinsic strength and failure behaviors of graphene grain boundaries, ACS Nano 6 (2012) 2704–2711.
[39] Z. Song, Y. Ni, Z. Xu, Geometrical distortion leads to Griffith strength reduction in graphene membranes, Extrem. Mech. Lett. 14 (2017) 31–37.
[40] P.Y. Huang, C.S. Ruiz-Vargas, A.M. van der Zande, W.S. Whitney, M.P. Levendorf, J.W. Kevek, S. Garg, J.S. Alden, C.J. Hustedt, Y. Zhu, J. Park, P.L. McEuen, D.A. Muller, Grains and grain boundaries in single-layer graphene atomic patchwork quilts, Nature 469 (2011) 389–392.
[41] P. Zhang, L. Ma, F. Fan, Z. Zeng, C. Peng, P.E. Loya, Z. Liu, Y. Gong, J. Zhang, X. Zhang, P.M. Ajayan, T. Zhu, J. Lou, Fracture toughness of graphene, Nat. Commun. 5 (2014) 3782.
[42] G. Jung, Z. Qin, M.J. Buehler, Molecular mechanics of polycrystalline graphene with enhanced fracture toughness, Extrem. Mech. Lett. 2 (2015) 52–59.
[43] J. Han, D. Sohn, W. Woo, D.K. Kim, Molecular dynamics study of fracture toughness and trans-intergranular transition in bi-crystalline graphene, Comput. Mater. Sci. 129 (2017) 323–331.
[44] M.A. Dewapriya, S.A. Meguid, Tailoring fracture strength of graphene, Comput. Mater. Sci. 141 (2018) 114–121.
[45] B. Jang, A.E. Mag-isa, J.H. Kim, B. Kim, H.J. Lee, C.S. Oh, T. Sumigawa, T. Kitamura, Uniaxial fracture test of freestanding pristine graphene using in situ tensile tester under scanning electron microscope, Extrem. Mech. Lett. 14 (2017) 10–15.
[46] T. Zhang, X. Li, H. Gao, Defects controlled wrinkling and topological design in graphene, J. Mech. Phys. Solid. 67 (2014) 2–13.
[47] D. Datta, S.P.V. Nadimpalli, Y. Li, V. Shenoy, Effect of crack length and orientation on the mixed-mode fracture behavior of graphene, Extrem. Mech. Lett. 5 (2015) 10–17.
[48] K. Kim, V.I. Artyukhov, W. Regan, Y. Liu, M.F. Crommie, B.I. Yakobson, A. Zettl, Ripping graphene: preferred directions, Nano Lett. 12 (2012) 293–297.
[49] I.A. Ovid'ko, Mechanical properties of graphene, Rev. Adv. Mater. Sci. 34 (2013) 1–11.
[50] T.H. Liu, C.W. Pao, C.C. Chang, Mechanical mutability of polycrystalline graphene from atomistic simulations, Comput. Mater. Sci. 91 (2014) 56–61.
[51] K.S. Kim, Y. Zhao, H. Jang, S.Y. Lee, J.M. Kim, K.S. Kim, J.H. Ahn, P. Kim, J.Y. Choi, B.H. Hong, Large-scale pattern growth of graphene films for stretchable transparent electrodes, Nature 457 (2009) 706–710.
[52] C. Lv, H. Yu, H. Jiang, Archimedean spiral design for extremely stretchable interconnects, Extrem. Mech. Lett 1 (2014) 29–34.
[53] S. Ling, Q. Wang, D. Zhang, Y. Zhang, X. Mu, D.L. Kaplan, M.J. Buehler, Integration of stiff graphene and tough silk for the design and fabrication of versatile electronic materials, Adv. Funct. Mater. 28 (2018) 1–10.
[54] Y.I. Jhon, S.E. Zhu, J.H. Ahn, M.S. Jhon, The mechanical responses of tilted and non-tilted grain boundaries in graphene, Carbon 50 (2012) 3708–3716.
[55] A. Cao, Y. Yuan, Atomistic study on the strength of symmetric tilt grain boundaries in graphene, Appl. Phys. Lett. 100 (2012) 13–16.
[56] Z. Yang, Y. Huang, H. Bao, K. Xu, F. Ma, Synergistic effects of grain boundaries and edges on fatigue deformations of sub-5 nm graphene nanoribbons, J. Mater. Sci. 52 (2017) 10871–10878.
[57] Y. Li, D. Datta, Z. Li, Anomalous mechanical characteristics of graphene with tilt grain boundaries tuned by hydrogenation, Carbon 90 (2015) 234–241.
[58] J. Han, S. Ryu, D. Sohn, S. Im, Mechanical strength characteristics of asymmetric tilt grain boundaries in graphene, Carbon 68 (2014) 250–257.
[59] O. V Yazyev, S.G. Louie, Topological defects in graphene: dislocations and grain boundaries, Phys. Rev. B 81 (2010) 1–7.
[60] S. Plimpton, Fast parallel algorithms for short-range molecular dynamics, J. Comput. Phys. 117 (1995) 1–19.
[61] S.J. Stuart, A.B. Tutein, J.A. Harrison, A reactive potential for hydrocarbons with intermolecular interactions, J. Chem. Phys. 112 (2000) 6472–6486.
[62] B. Wang, Y. Puzyrev, S.T. Pantelides, Strain enhanced defect reactivity at grain boundaries in polycrystalline graphene, Carbon 49 (2011) 3983–3988.
[63] M.C. Wang, C. Yan, L. Ma, N. Hu, M.W. Chen, Effect of defects on fracture strength of graphene sheets, Comput. Mater. Sci. 54 (2012) 236–239.
[64] J. Li, B. Ni, T. Zhang, H. Gao, Phase field crystal modeling of grain boundary structures and growth in polycrystalline graphene, J. Mech. Phys. Solid. 120 (2018) 36–48.
[65] P. Hirvonen, M.M. Ervasti, Z. Fan, M. Jalalvand, M. Seymour, S.M. Vaez Allaei, N. Provatas, A. Harju, K.R. Elder, T. Ala-Nissila, Multiscale modeling of polycrystalline graphene: a comparison of structure and defect energies of realistic samples from phase field crystal models, Phys. Rev. B 94 (2016) 1–17.
[66] J.M. Carlsson, L.M. Ghiringhelli, A. Fasolino, Theory and hierarchical calculations of the structure and energetics of [0001] tilt grain boundaries in graphene, Phys. Rev. B Condens. Matter 84 (2011) 1–10.
[67] J. Zhang, J. Zhao, Structures and electronic properties of symmetric and nonsymmetric graphene grain boundaries, Carbon 55 (2013) 151–159.
[68] A. Cao, J. Qu, Atomistic simulation study of brittle failure in nanocrystalline graphene under uniaxial tension, Appl. Phys. Lett. 102 (2013) 1–6.
[69] K.K. Shih, J.C. Li, Energy of grain boundaries between cusp misorientations, Surf. Sci. 50 (1975) 109–124.
[70] J.C.M. Li, Disclination model of high angle grain boundaries, Surf. Sci. 31 (1972) 12–26.
[71] J.D. Eshelby, A simple derivation of the eastic field of an edge dislocation, Br. J. Appl. Phys. 17 (1966) 1131.